Temperature compensation of the fiber-optic based system for the shape reconstruction of a minimally invasive surgical needle

Aizhan Issatayeva, Aida Amantayeva, Wilfried Blanc, Carlo Molardi, Daniele Tosi

Temperature compensation of the fiber-optic based system for the shape reconstruction of a minimally invasive surgical needle

Aizhan Issatayeva [a,*], Aida Amantayeva [a], Wilfried Blanc [b], Carlo Molardi [a], Daniele Tosi [a,c]

[a] Department of Computer and Electrical Engineering, Nazarbayev University, Kabanbay Batyr, Nur-Sultan 010000, Kazakhstan
[b] Université Côte d'Azur, INPHYNI – CNRS UMR 7010, Parc Valrose, 06108 Nice, France
[c] Laboratory of Biosensors and Bioinstruments, National Laboratory of Astana, Kabanbay Batyr, Nur-Sultan 010000, Kazakhstan

ARTICLE INFO

Article history:

Keywords:
Distributed sensing
Fiber optic sensors
Medical needle
Minimally invasive surgery
OBR
Shape reconstruction
Temperature compensation

ABSTRACT

This paper presents the methodology for temperature compensation of a system for shape reconstruction of a minimally invasive surgical needle. The system is based on four optical fibers glued along the needle at 90° from each other and connected to the optical backscattering reflectometry interrogator. The interrogator measures backscattered light from four fibers, which shifts as a response to temperature or strain variations. During minimally invasive surgery the fibers sense both the strain change (due to the needle bending) and the temperature change (due to the difference between the temperature of the environment and the human body). Shape reconstruction is based on the strain measurements, so the temperature readings need to be compensated. The methodology of compensation is based on the two pairs of opposite fibers, which measure the same temperature change and opposite strain. The spectral shifts of the opposite fibers are added to find only the temperature component and the result is subtracted from the whole spectral shift to find the strain change detected by each fiber. This method has been validated by repeated constant insertion into a temperature-varying phantom. The algorithm has succeeded in the extraction of the strain component, which found to be the same in all trials despite the changing temperature.

1. Introduction

Shape sensing technologies have been increasingly reported as an important application for sensors [1–3]. The measurement of shape in real-time has a significant impact in medical applications because it allows precise monitoring of the insertion and positioning of percutaneous and endoscopic catheters [4], as well as performing some diagnostic directly from the shape characteristics, particularly in cardiovascular detection [5]. Radiation and imaging-based methods have been strongly documented, however, they have significant drawbacks in terms of speed, precision, and the requirement to support the detection with additional equipment. For this reason, in recent times we have witnessed the surge of fiber-optic shape sensing methods, that make use of optical fibers in order to perform a real-time, *in situ* shape sensing [4,5].

The first area of application of shape sensing is in endoscopic devices, which are catheters inserted through anatomic channels with semi-flexible form factor [4–6]. These types of catheters are usually based on expansile material such as nitinol or flexible plastic [6], and experience significant bending when inserted into place. For example, Al-Hamad et al. [4] reported a case study of a 3D-printed catheter tube bent over curvature values around 0.67 cm^{-1}, while Khan et al. [6] reported curvature sensing within 0.002 mm^{-1} up to 0.02 mm^{-1}.

The most prominent technology for shape sensing of semi-flexible devices is based on fiber Bragg gratings (FBGs), and specifically FBGs in multicore fibers (MCFs) [7,8]. FBGs are narrow-band reflectors that can be inscribed in-line into each core of an MCF [9]. When torsions are applied to the fiber, the differential wavelength shift recorded by each FBG is converted to a 3-dimensional strain through a pre-defined model, such as the Frenet-Serret model [3] or the transformation matrix [8], both having an efficient computation. The method of the inscription of FBGs in MCFs allows achieving a tight spatial resolution since FBG arrays with sub-centimeter spacing have been consistently reported [9].

The application of shape sensing technologies in rigid percutaneous needles represents a different case scenario: percutaneous devices have high stiffness, that sustains a penetration through the skin and several layers of tissues, which requires devices that detect small lateral bending, usually around few millimeters for a needle of few centimeters. Given that the rigid structure of the needle contrasts the deformations, MCF devices are unsuitable for performing

* Corresponding author.
E-mail address: aizhan.issatayeva@nu.edu.kz (A. Issatayeva).

a shape reconstruction as they do not have enough accuracy. Rigid applicators are an important case for investigation since they can be applied in several therapeutic and anesthetic procedures, such as in the monitoring of Chiba percutaneous needles [2] for thermotherapies, or Tuohy needles for epidural anesthesia [10]. Currently, guidance systems for percutaneous insertions of the rigid needles are based on a single FBG [11–13], which determines the pressure level at the target tissue, but does not render the whole process of insertion from the skin to the target zone.

The 3-dimensional needle's shape monitoring during the whole process of insertion can be performed using distributed sensing, and in particular, the method based on optical backscattering reflectometry (OBR) [14]. The OBR detects the Rayleigh scattering signatures of fibers in the frequency domain, along the whole fiber link, and therefore it can measure distributed strain; by using multiple fibers, strain measurements can be extended to shape. Parent et al. [2] proposed a triplet of fiber forming an equilateral triangle within the walls of the needle, while Beisenova et al. [10] proposed a method based on a fiber quadruplet fixed outside of an epidural device. The last method is particularly interesting because this external mount does not obstruct the flow of the anesthetic fluid inside the device, and therefore it is compatible with any hollow anesthetic needle. This shape sensing method reported for rigid epidural needles have typical curvature around $10^{-5}\,\mathrm{mm}^{-1}$ [10].

One of the drawbacks of OBR methods for shape sensing is that each strain measurement is influenced by temperature; in fact, the fibers have a dual sensitivity to strain and temperature (about 1 pm/$\mu\varepsilon$ and 10 pm/°C at 1550 nm). When the needle is inserted into the tissue, part of the fiber is exposed at room temperature, while the inner part is exposed to the body temperature, around 36 °C; this corresponds to a temperature differential between the tip and the tail of the needle of about 10–15 °C (depending on ambient temperature). Moreover, in the case of epidural anesthesia, the needle pierces through multiple layers of tissues with different consistency, and therefore the onboard sensors are sensitive to both the transition between ambient temperature and inner body temperature, as well as to the local variations of each subcutaneous layer [15].

Floris et al. [16] have recently reviewed 3D shape sensing methods based on optical fibers (FBGs, MCFs, and OBR) and mentioned some temperature compensation techniques. Most previous shape sensing works reported for medical devices have been performed on lab phantoms held at room temperature [10,17,18], or for guidance and endoscopic systems that are entirely inserted *in situ* and therefore do not experience any inner-outer temperature variation [19–21]. The existing temperature compensation methods are based on the transfer matrix [8] or the Frenet-Serret algebra [3] that work only for large bending and are suitable for semi-flexible devices.

In this work, we report a method for temperature compensation in shape sensing of a rigid epidural needle, based on a fiber quadruplet mounted at the four cardinal points of a Tuohy needle. This method has been calibrated on a hot phantom, inserting the needle with a linear actuator, and using an estimation of the thermal data in each section of the fiber to remove thermal effects from the shape estimation in each needle section. This method has been validated on a hot phantom, allowing a simple yet effective improvement for *in vivo* shape sensing of percutaneous devices.

2. Material and methods

2.1. Shape reconstruction system working principle

According to Fig. 1(a), the system for the shape reconstruction of the needle is achieved by equipping the Tuohy needle with four optical fibers connected through the 1 by 4 coupler to the Luna OBR (Luna OBR 4600, Luna Inc., USA) interrogator. The interrogator detects the light scattered from each small section of the fiber and measures its spectral shift resulted from the strain or temperature application [2]. The spectral shift has a linear relationship with the strain and temperature changes when they are applied separately, therefore the interrogator provides distributed measurements of these parameters with a high resolution (0.2 cm in this paper). The fibers are glued outside the needle at 90° from each other (Fig. 1(b)), so that two pairs of opposite fibers are created (left and right, upper and lower). The distributed strain detected by each pair of the fibers is used to reconstruct the needle shape along the two perpendicular axes (X and Y) which allows detection and visualization of the needle bending to all directions. The simultaneous scan of all fibers is reached by using scattering level multiplexing, which is based on two types of fibers: standard single-mode fibers (SMF) and high-scattering MgO nanoparticles doped fibers (NPDF) [22,23]. NPDFs, which have a backscattering level of 35–40 dB higher than SMFs, are spliced with SMF pigtails which lengths are selected in such a way that each SMF is about 10 cm longer than the previous SMF+NPDF fiber (Fig. 1(d)). As a result, the neighboring NPDFs are spatially separated from each other (Fig. 1(c)) and can be used as sensing fibers. The system for shape reconstruction has shown promising results during the insertion into a custom-made phantom modeling the anatomy of the human body [10,17].

In the previous experiments, the phantom was at room temperature (about 25 °C), but in real life, the temperature of the human body can be about 35.5–39.6 °C [24]. Therefore, some part of the spectral shift detected by the interrogator will be caused by the strain change due to the needle bending, while another part will correspond to the temperature difference between the environment and the human body. To achieve an accurate shape reconstruction system, it is important to extract the strain component of the spectral shift. The temperature compensation technique has been developed by the following steps:

(1) Application of the varying temperature (keeping strain constant) and varying strain (keeping temperature constant) to the NPDFs to find the temperature and strain coefficients (Section 2.2).
(2) Application of the varying temperature (keeping strain constant) and varying strain (keeping temperature constant) to the sensorized needle to identify the behavior of the system when only one of the external changes is applied (Sections 2.3 and 2.4).
(3) Application of the varying temperature and strain at the same time to the sensorized needle to design the temperature compensation method (Section 2.5).

2.2. Finding temperature and strain coefficients

In order to convert the spectral shift detected by the interrogator to the applied strain or temperature, the respective coefficients need to be found. The temperature coefficient has been estimated by immersing the NPDF into a water bath which has been heated from 33 °C to 95 °C by a hot plate [25]. Fig. 2(a) illustrates the linear relationship between the detected spectral shift and the applied temperature, and the temperature coefficient was found to be $k_T = -1.005\,\mathrm{GHz/°C}$. In the strain calibration experiment, about 1.5 m of the NPDF has been locked in between two micropositioners, which applied the strain change from 0 $\mu\varepsilon$ to 900 $\mu\varepsilon$ [25]. According to Fig. 2(b), the spectral shift has changed linearly in response to the applied strain and the strain coefficient is $k_\varepsilon = -0.1298\,\mathrm{GHz}/\mu\varepsilon$.

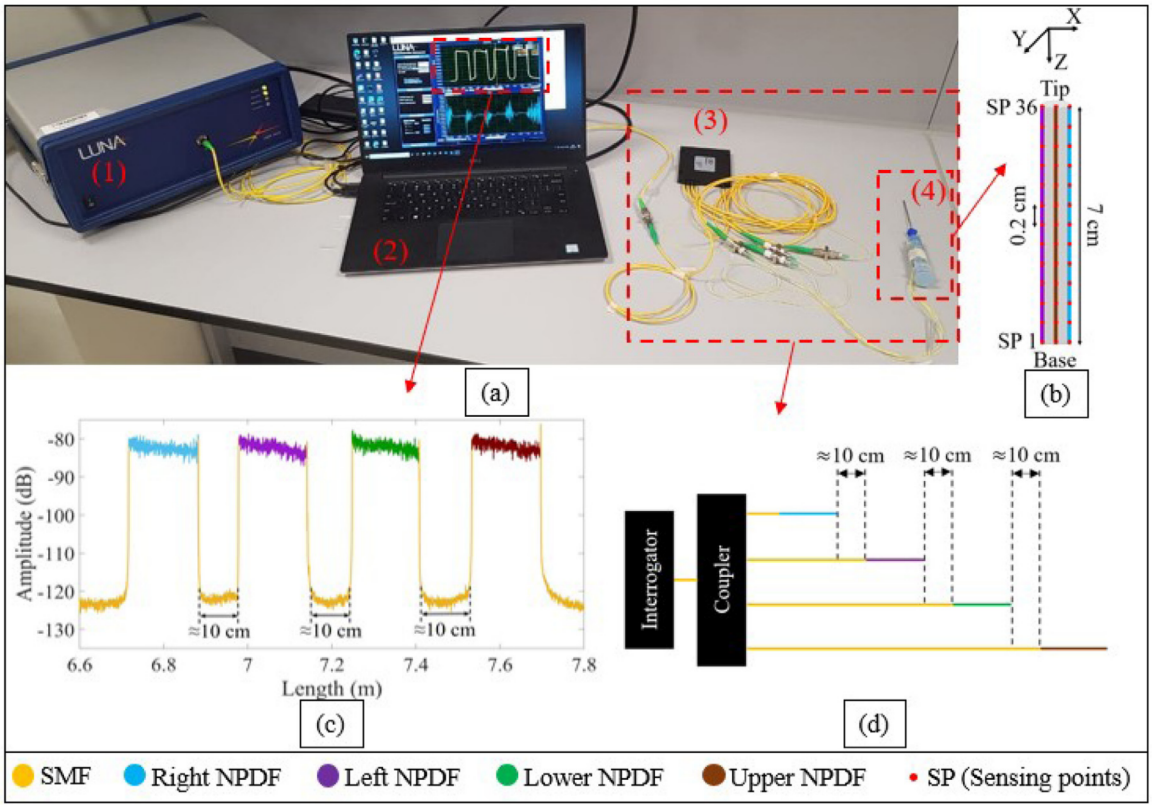

Fig. 1. The shape reconstruction setup (a) consists of the interrogator (1) with the evaluation software (2), connected through the coupler (3) to four NPDF+SMF fibers glued along the Tuohy needle (4). The schematics of the fibers arrangement along the needle is shown in (b). The spectrum of the backscattering light of four NPDF+SMF fibers is shown in (c) and the schematics of multiplexing methodology is given in (d).

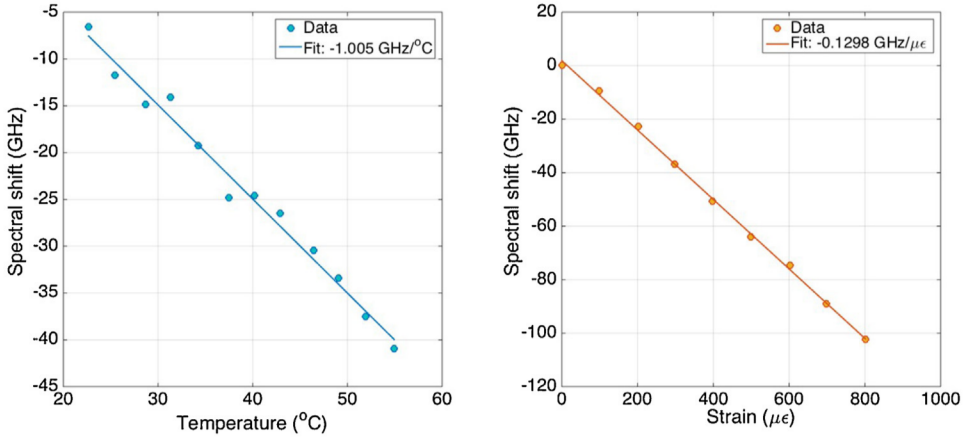

Fig. 2. Temperature (a) and strain (b) effect on the spectral shift of the backscattered light along the NPDF.

2.3. Experiment with the varying temperature

In the experiment with varying temperature, the needle has been put in a fixed position into the temperature chamber and has been heated from 25 °C to 40 °C with a step of 3 °C. There was no strain change applied to the fibers, therefore the spectral shift detected by the OBR has been converted to the temperature change with the coefficient $k_T = -1.005$ GHz/°C. According to Fig. 3, the temperature detected by the four fibers does not exactly correspond to the temperature measured by the thermocouple because it detects the temperature inside the thermal camera, not the needle or the fibers. This is done in order not to touch the needle and the fibers with the thermocouple. However, the recorded temperature change is increasing with a growth of applied temperature and the pattern for all four fibers is the same. Thus, all four fibers feel the same temperature when the heat is applied to the needle.

2.4. Experiment with the varying strain

In the experiment with varying strain, the needle's base has been fixed while its tip has been shifted to the direction of the lower fiber (along the Y-axis) from 0 cm to 1 cm with a step of 0.1 cm. The temperature of the needle and fibers have been kept constant, so the spectral shift has been converted to strain by the coefficient $k_\varepsilon = -0.1298$ GHz/$\mu\varepsilon$. Fig. 4 shows the strain change detected by each of the four fibers during this experiment. The pair of the upper

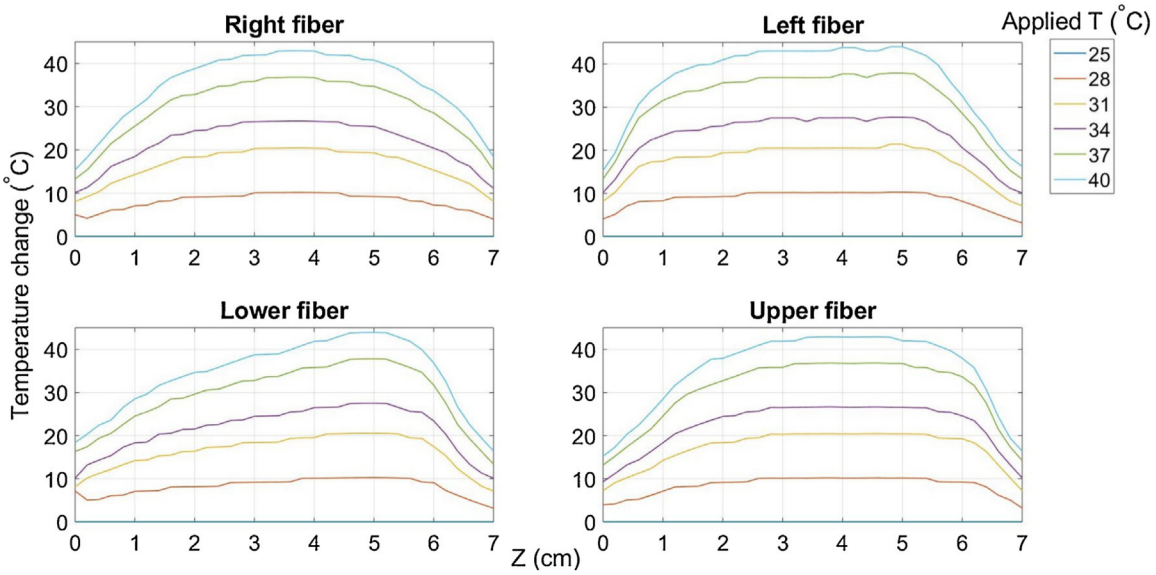

Fig. 3. Temperature detected by each of the four fibers around the needle during the heating of the needle from 25 °C to 40 °C with a step of 3 °C.

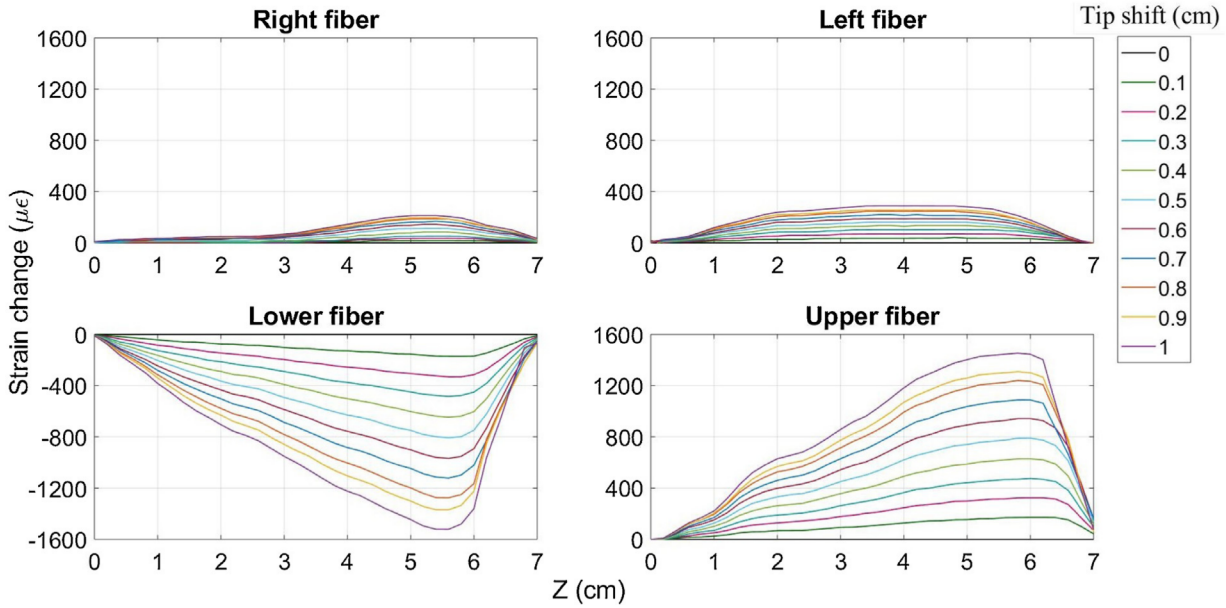

Fig. 4. Strain detected by each of the four fibers around the needle during the needle's tip shift to the lower direction from 0 cm to 1 cm with a step of 0.1 cm.

and lower fibers has detected almost the same strain but with opposite signs because the lower fiber has been compressed and the upper fiber feels tension. The needle has not been bent along the *X*-axis, so the pattern for the left-right fibers is different. They have detected similar strain with the same sign, but much smaller than the pair of the upper-lower fibers. This can be explained by the fact that the two fibers still experience some bending because they are attached to the needle. The needle has been bent to all other main directions (upper, left, and right) and to four intermediate directions as well (upper-left, upper-right, lower-left, and lower-right) and those results are presented in another paper. The conclusion from the set of strain calibration experiments is the following:

- If the bending is present along the *X*-axis or/and *Y*-axis, the pair of the left-right or/and upper-lower fibers detect similar large strain (about 100–150 $\mu\varepsilon$) but with opposite sign.
- If the bending is absent along the *X*-axis or *Y*-axis, the pair of the left-right or upper-lower fibers detect similar small strain (about 20–30 $\mu\varepsilon$) with the same sign.

2.5. Experimental setup for temperature compensation

Fig. 5shows that the previous experimental setup (1–4) has been supplemented with the temperature compensation unit consisting of the linear actuator (5), the sausage phantom (6), the temperature chamber (7), the thermocouple (8), and the thermal camera (9). The sausage is applied as a phantom because the custom-made phantom used in the previous experiments [10,17] contains jelly, which melts with the temperature increase. Moreover, the simplicity of the phantom can be an advantage to have a more uniform temperature distribution, which has been checked by the thermal camera. The phantom has been placed into a temperature chamber and heated from 25 °C (room temperature) to 40 °C (high body

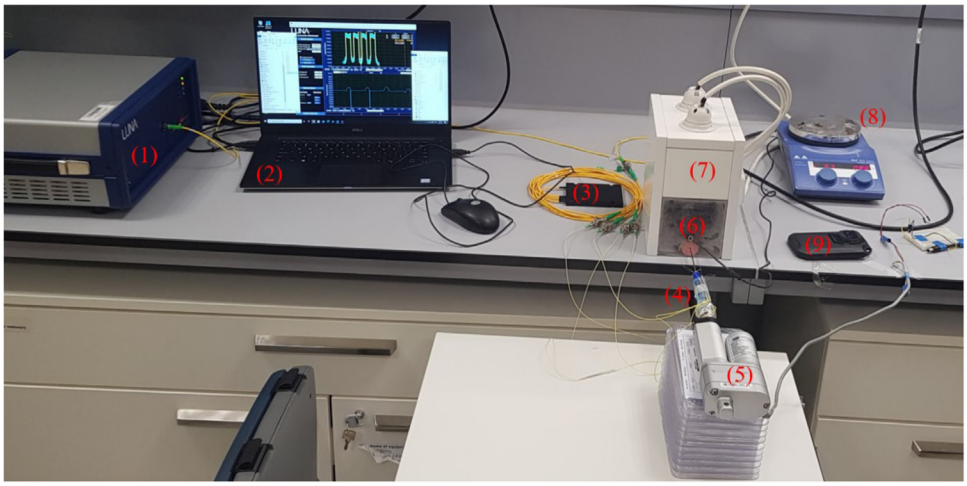

Fig. 5. Experimental setup consists of the interrogator (1), the evaluation software (2), the coupler (3), the needle with four NPDF+SMF (4). The needle is attached to the linear actuator (5) to achieve repeated insertions into the sausage phantom (6). The phantom is heated inside the temperature chamber (7) from 25 °C to 40 ° and its temperature is measured by the thermocouple (8) and the thermal camera (9).

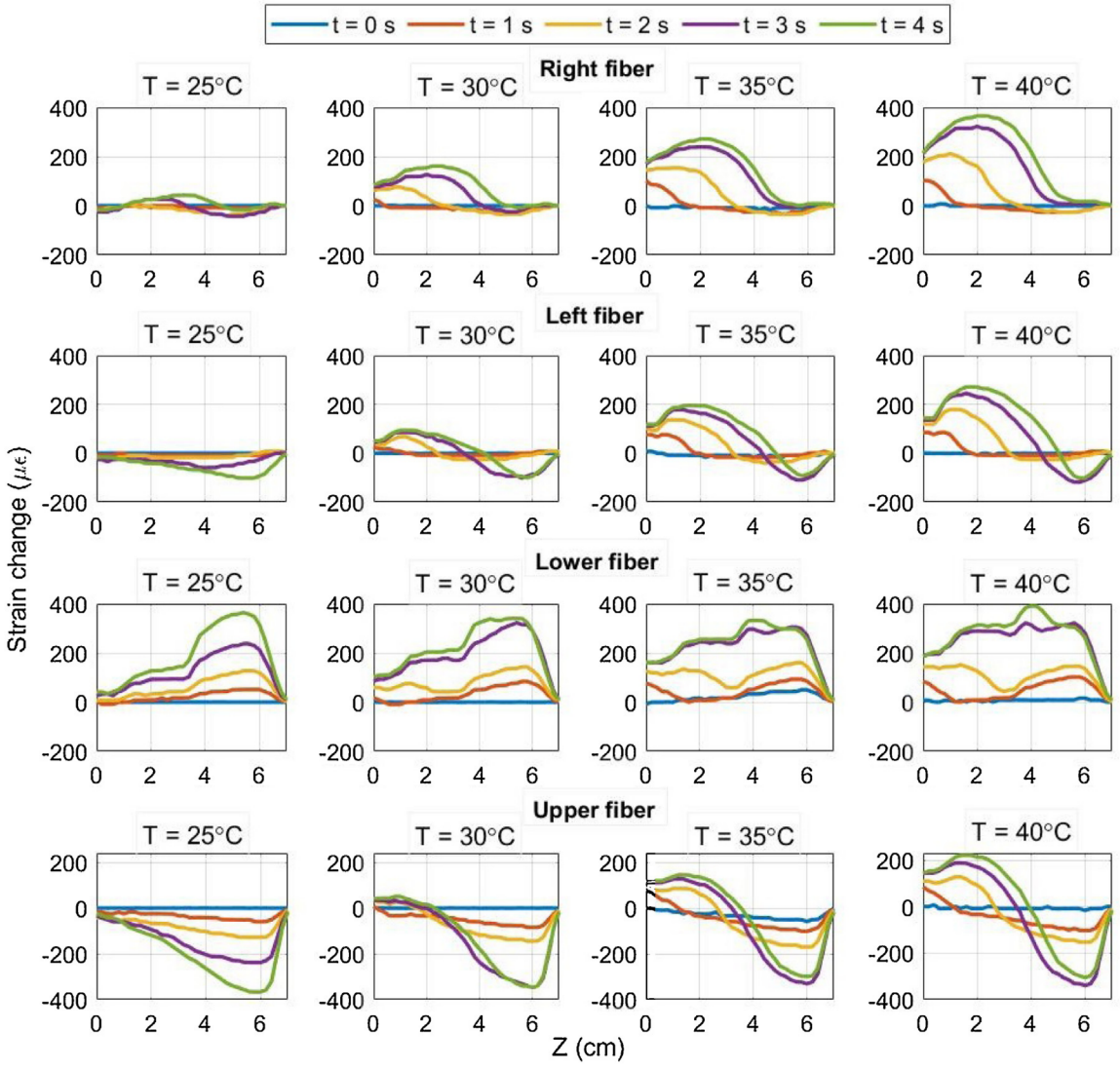

Fig. 6. Strain of each fiber retrieved from the originally recorded spectral shift.

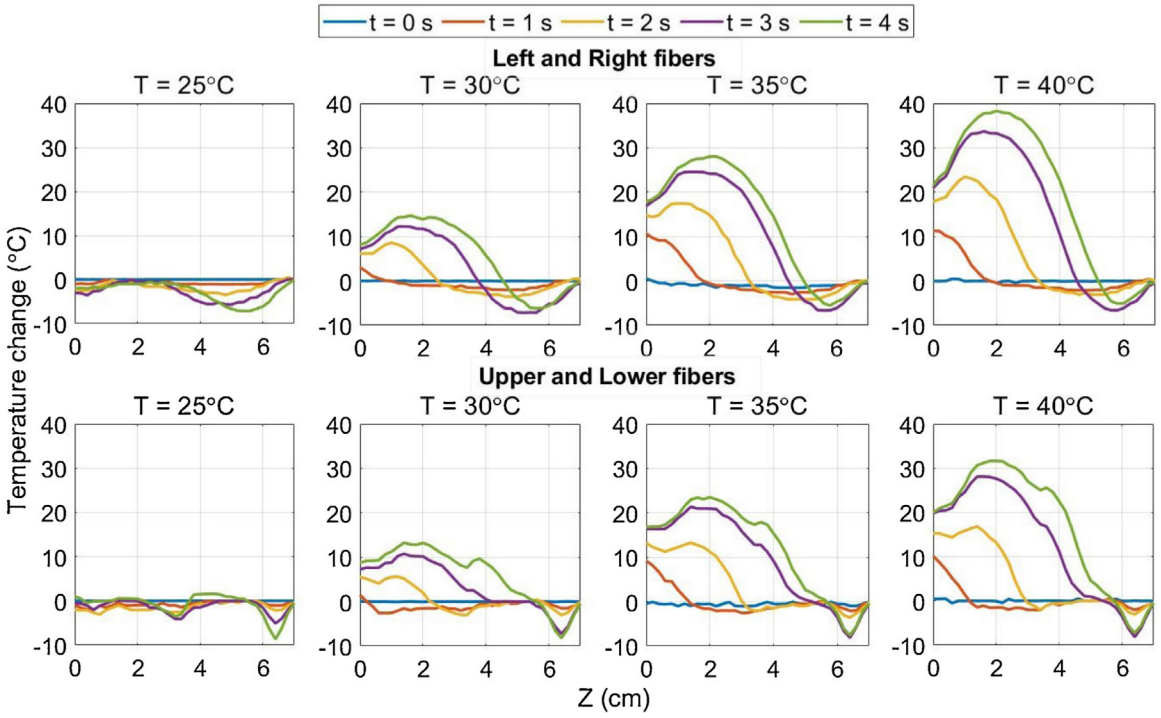

Fig. 7. Temperature of each fiber retrieved from the spectral shift using the temperature compensation algorithm.

temperature). The temperature of the sausage has been monitored by the thermocouple, then each 5 °C the needle has been inserted into the sausage and the spectral shift has been recorded by the OBR interrogator. In order to reach the same strain change in each trial, the needle has been inserted in the same way with the same speed using a linear actuator (Glideforce LACT2P-12V-20 Light-Duty, Concentric International, USA). The linear actuator moved the needle by 5 cm with a speed of about 1.5 cm/s. The movement was expected to be straightforward, but it was noticed that the needle has been moved a little upward.

This setup allows comparing the spectral shift detected by the interrogator during constant needle insertions into the phantom at different temperatures (25 °C, 30 °C, 35 °C, 40 °C).

2.6. Algorithm for temperature compensation

The aim of this algorithm is to separate part of the spectral shift caused by the strain change ($f_{\varepsilon_{left}}$, $f_{\varepsilon_{right}}$, $f_{\varepsilon_{lower}}$, and $f_{\varepsilon_{upper}}$) from the whole recorded spectral shift (f_{left}, f_{right}, f_{lower}, and f_{upper}). The algorithm has been implemented in MATLAB (Mathworks, UK) and consists of the following steps:

(1) The temperature components of the spectral shifts of the pair of opposite fibers ($f_{T_{left}}$ and $f_{T_{right}}$, $f_{T_{lower}}$ and $f_{T_{upper}}$) can be found by finding an average of their spectral shifts:

$$f_{T_{right}} = f_{T_{left}} = (f_{left} + f_{right})/2$$
$$f_{T_{lower}} = f_{T_{upper}} = (f_{lower} + f_{upper})/2$$

According to the experiment with varying strain (Fig. 4), the needle bending causes two opposite fibers to detect the same strain (and spectral shifts) but with different sign. Therefore, when the spectral shifts of opposite fibers are added together, the strain components cancel each other and the only part left is the spectral shift resulted from the temperature change detected by the two fibers. The temperature component of each fiber can be found by dividing this sum by two, because all four fibers have the same sensitivity to temperature variation (Fig. 3).

(2) The spectral shift found in the step 1 can be converted to the temperature change in °C by dividing it by the coefficient $k_T = -1.005$ GHz/°C:

$$T_{left} = T_{right} = f_{T_{left}}/k_T$$
$$T_{lower} = T_{upper} = f_{T_{lower}}/k_T$$

The temperature found for each fiber is shown in Section 3 (Fig. 7).

(3) Spectral shift responsible for strain has been found by subtracting the temperature component from the total spectral shift:

$$f_{\varepsilon_{left}} = f_{left} - f_{T_{left}}$$
$$f_{\varepsilon_{right}} = f_{right} - f_{T_{right}}$$
$$f_{\varepsilon_{lower}} = f_{lower} - f_{T_{lower}}$$
$$f_{\varepsilon_{upper}} = f_{upper} - f_{T_{upper}}$$

(4) The strain has been found by dividing each spectral shift from the step 3 by the coefficient $k_\varepsilon = -0.1298$ GHz/$\mu\varepsilon$:

$$\varepsilon_{left} = f_{\varepsilon_{left}}/k_\varepsilon$$
$$\varepsilon_{right} = f_{\varepsilon_{right}}/k_\varepsilon$$
$$\varepsilon_{lower} = f_{\varepsilon_{lower}}/k_\varepsilon$$
$$\varepsilon_{upper} = f_{\varepsilon_{upper}}/k_\varepsilon$$

The strain change found for each fiber is shown in Section 3 (Fig. 8).

(5) The strain retrieved from the spectral shift is used to reconstruct the shape of the needle. Each fiber is divided by $n = 36$ sensing points into 35 sections (see Fig. 1(b)). The needle bending causes some of the fibers to elongate, while the opposite fibers to compress. The changed length of each ith section of the fibers (S_{left_i}, S_{right_i}, S_{lower_i}, and S_{upper_i}) can be found by multiplying the length of

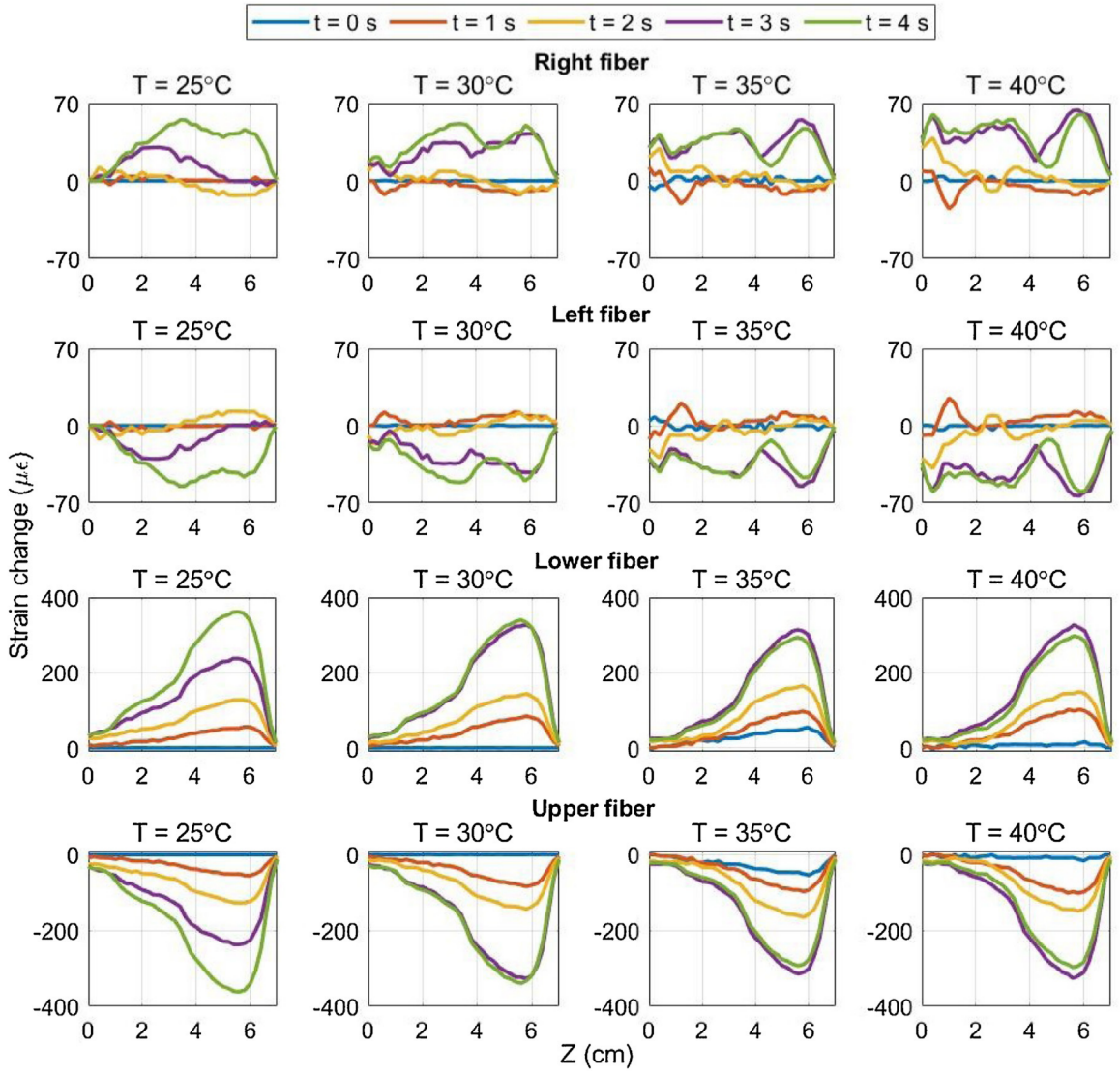

Fig. 8. Strain of each fiber retrieved from the originally the spectral shift after temperature compensation.

each section ($s = 0.2$ cm) by the average of strains detected by the neighboring sensing points:

$$\begin{aligned} S_{left_i} &= s + s \times (\varepsilon_{left_i} + \varepsilon_{left_{i+1}})/2 \\ S_{right_i} &= s + s \times (\varepsilon_{right_i} + \varepsilon_{right_{i+1}})/2 \\ S_{lower_i} &= s + s \times (\varepsilon_{lower_i} + \varepsilon_{lower_{i+1}})/2 \\ S_{upper_i} &= s + s \times (\varepsilon_{upper_i} + \varepsilon_{upper_{i+1}})/2 \end{aligned}$$

The bending angle, which is an angle of inclination of each section of the needle along the X and Y axes, is found by dividing the difference between the lengths of the previous sections of the opposite fibers by the diameter of the needle ($d = 0.127$ cm):

$$\begin{aligned} \beta_{lr_{i+1}} &= \beta_{lr_i} + \arctan((S_{left_i} - S_{right_i})/d) \\ \beta_{ul_{i+1}} &= \beta_{ul_i} + \arctan((S_{upper_i} - S_{lower_i})/d) \end{aligned}$$

The bending angles of the first section are $\beta_{lr_1} = 0$ and $\beta_{ul_1} = 0$. The x, y, z coordinates of the sensing points along all four fibers are found by the following equations:

$$\begin{aligned} x_{left_{i+1}} &= x_{left_i} + S_{left_i} \times \sin(\beta_{lr_i}) \\ x_{right_{i+1}} &= y_{right_i} + S_{right_i} \times \sin(\beta_{lr_i}) \\ z_{left_{n-i-1}} &= z_{left_{n-i}} + S_{left_i} \times \cos(\beta_{lr_i}) \\ z_{right_{n-i-1}} &= z_{right_{n-i}} + S_{right_i} \times \cos(\beta_{lr_i}) \\ y_{lower_{i+1}} &= y_{lower_i} + S_{lower_i} \times \sin(\beta_{ul_i}) \\ y_{upper_{i+1}} &= y_{upper_i} + S_{upper_i} \times \sin(\beta_{ul_i}) \\ z_{lower_{n-i-1}} &= z_{lower_{n-i}} + S_{lower_i} \times \cos(\beta_{ul_i}) \\ z_{upper_{n-i-1}} &= z_{upper_{n-i}} + S_{upper_i} \times \cos(\beta_{ul_i}) \end{aligned}$$

The coordinates of the first sensing points (SP1) are: $x_{left_1} = -\frac{d}{2}$, $x_{right_1} = \frac{d}{2}$, $z_{left_n} = 0$, $z_{right_n} = 0$, $y_{lower_1} = -\frac{d}{2}$, $y_{upper_1} = \frac{d}{2}$, $z_{lower_n} = 0$, $z_{upper_n} = 0$.

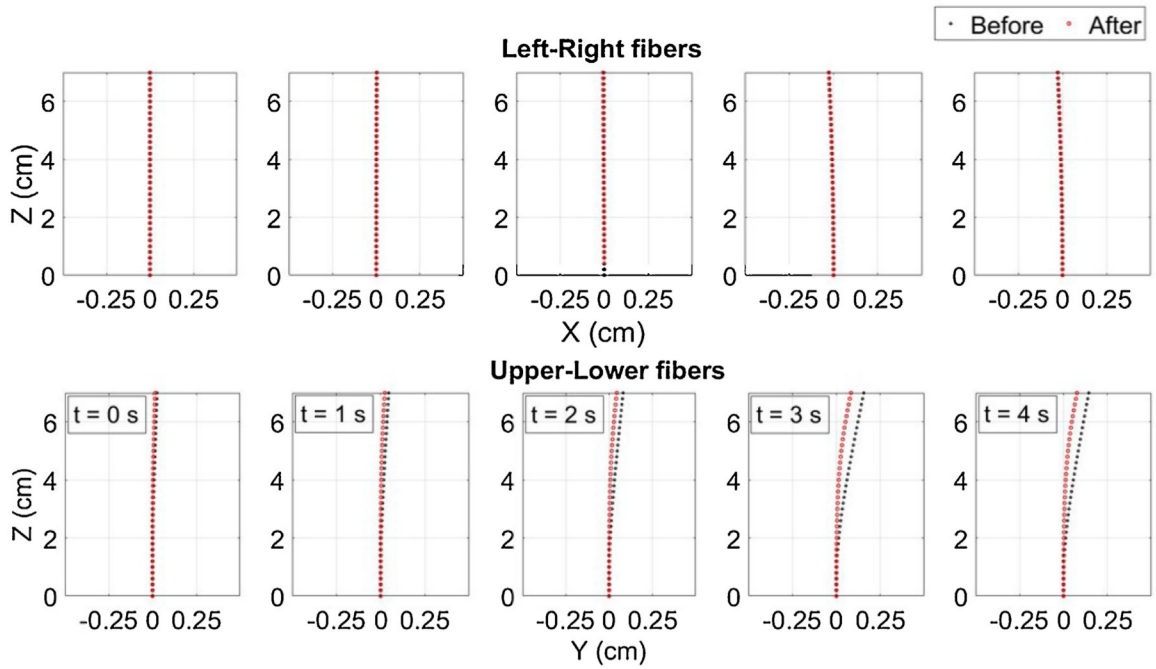

Fig. 9. Reconstruction of the needle shape during its insertion into the phantom at 35 °C after temperature compensation.

Finally, the average of the x-coordinates of the left and right fibers is taken to find the x-coordinates of the middle of the needle, and its y-coordinates are found by calculating the average of the upper-lower fibers' y-coordinates. The average of the z-coordinates of all four fibers is used to find the z-coordinates of the middle of the needle. The coordinates have been multiplied by the coefficient found from the needle calibration experiment: $1.39295 \times x + 1.91441$ for the left-right fibers and $1.25813 \times y + 1.54276$ for the upper-lower fibers. Fig. 9 illustrates the middle of the needle reconstructed by the aforementioned algorithm during the needle insertion into the sausage at 35 °C (the closest to the body temperature).

3. Results and discussion

3.1. Strain and shape reconstruction before the temperature compensation

The needle insertion into the phantom lasted for 4 seconds and the temperature of the phantom was 25 °C, 30 °C, 35 °C, and 40 °C. Fig. 6 illustrates the strain per length of each fiber at each second for all four temperatures of the phantom resulted by converting the recorded spectral shift. The pattern for all four fibers is different from the one shown in Fig. 4: the pairs of opposite fibers detect nor similar neither opposite patterns. This is one of the possible signs that the strain pattern is not correct and there is an influence of the temperature.

3.2. Temperature compensation

Fig. 7 illustrates the temperature of all four fibers that has been extracted from the spectral shift by using the temperature compensation algorithm. First of all, the pattern is similar for all fibers: the detected temperature is increasing with the growth of the phantom temperature. Moreover, since the needle is inserted with a speed of 1.5 cm/s, the part of the needle inside the phantom can be tracked based on the temperature pattern. At the 1st second about 1.5 cm of the needle detects the temperature increase due to the location inside the phantom (red line), at the subsequent 2nd–3rd seconds 3 cm (orange line) and 4.5 cm (purple line) of the needle are influenced by the phantom's temperature. Since the linear actuator has moved the needle by 5 cm, at the last second 5 cm of the needle detects raised temperature (green line). It can be also noticed that the temperature recorded by the left and right fibers is a little higher than that measured by the pair of the upper-lower fibers. This is because the pair of the left-right fibers should detect small strain with the same sign due to the absence of the needle bending along the X-axis. As a result, the strain components of their spectral shifts have not canceled during the temperature compensation and is included in the temperature reconstruction. Thus, the algorithm can also be used to compensate for this small strain detected by the fibers along which there was no bending.

3.3. Strain and shape reconstruction after the temperature compensation

Fig. 8 depicts the strain of each fiber retrieved from the spectral shift after the temperature has been compensated. As can be seen, the opposite fibers have detected similar strain with opposite signs. Moreover, the strain pattern is almost the same for all temperatures of the phantom, because the needle has been inserted in the same way in all trials of the experiments and the temperature of the phantom should not influence the strain sensed by the fibers.

The reconstruction of the needle along the X and Y axes during its insertion into the phantom at 35 °C (the closest to the normal body temperature) before (black) and after (red) the temperature compensation is shown in Fig. 9. As can be seen, the needle shift along the X-axis is very small both before and after compensation because the needle bending to the left-right directions was negligible. As it has been mentioned the needle moved upwards a little bit, so the algorithm has detected the bending along the Y-axis. In the before compensation scenario, at each second of the insertion the needle's tip has been shifted by 0.045 cm, 0.081 cm, 0.155 cm,

0.143 cm, while after the temperature has been compensated the tip has been moved by 0.024 cm, 0.044 cm, 0.083 cm, and 0.076 cm. Therefore it can be seen that in the first case the needle bending has been almost twice overestimated due to the influence of the temperature.

The shape reconstruction shown in Fig. 9 makes an effective demonstration that the multi-fiber sensing method can compensate temperature spatial variations, which include both the ambient-to-body temperature transition and the inner local temperature variations, using the same fibers already in place for the shape determination. This possibility is an important feature in the clinical implementation of shape sensing of a percutaneous device which pierces through several layers of tissues, and was hereby validated with a dedicated phantom that emphasizes the local temperature transitions.

4. Conclusion

The system for the needle shape reconstruction has shown promising results in the experiments with the custom-made phantom. However, in the real clinical surgeries, the temperature difference between the human body and the environment should be taken into account. Therefore, this paper has presented the methodology to compensate for the temperature influence as well as for the small strain detected by the fibers when there was no bending along their axis. This compensation has been achieved because of the arrangement of fibers: four fibers at 90° from each other to create two pairs of opposite fibers. This arrangement has been used both for the shape reconstruction algorithm and for the temperature compensation because the opposite fibers detect the same temperature and the same strain but with opposite signs. This allows canceling out the strain or temperature components by manipulating the spectral shifts of two opposite fibers. The temperature compensation algorithm can be used to accurately reconstruct the shape of the needle without the influence of the temperature and also to track the needle's position inside the human body. The tracking is based on the pattern of the reconstructed temperature, where it can be seen which part of the needle experiences higher temperature. The fibers are glued outside of the needle, which allows delivering a liquid through a needle without any obstacles and thus, use the needle for drug and anesthetic delivery (*i.e.* epidural anesthesia). A similar system with some adjustments can be used to reconstruct the shape and compensate the temperature for other types of minimally invasive rigid surgical devices.

Author contributions

A.I. contributed to the setup development, conduction of the experiment, data analysis and paper writing, A.A. contributed to the conduction of the experiment, W.B. drew the NPDF fibers, C.M. supervised the setup preparation and data analysis, D.T. contributed to the paper writing, supervised the setup preparation, data analysis, paper writing and editing.

Declaration of competing interest

The authors report no declarations of interest.

Acknowledgements

The research is funded by Nazarbayev University, under grants FOSTHER (code: 090118FD5314), EPICGuide (code: 240919FD3908), SMARTER (code: 091019CRP2117). The authors would like to also acknowledge the support of NPO Young Researchers Alliance and Nazarbayev University Corporate Fund "Social Development Fund" for grant under their Fostering Research and Innovation Potential Program. The authors would like to thank Pr. Zhanat Kappassov and Mr. Temirlan Galimzhanov (School of Engineering and Digital Sciences, Robotics and Mechatronics, Nazarbayev University, Nur-Sultan, Kazakhstan) for their help in this project.

References

[1] P. Westbrook, T. Kremp, K. Feder, W. Ko, E. Monberg, H. Wu, D. Simoff, T. Taunay, R.M. Ortiz, Continuous multicore optical fiber grating arrays for distributed sensing applications, J. Lightwave Technol. 35 (6) (2017) 1248–1252.
[2] F. Parent, S. Loranger, K.K. Mandal, V.L. Iezzi, J. Lapointe, J.S. Boisvert, M.D. Baiad, S. Kadoury, R. Kashyap, Enhancement of accuracy in shape sensing of surgical needles using optical frequency domain reflectometry in optical fibers, Biomed. Opt. Express 8 (4) (2017) 2210–2221.
[3] I. Floris, J. Madrigal, S. Sales, J. Adam, P. Calderón, Experimental study of the influence of FBG length on optical shape sensor performance, Opt. Lasers Eng. 126 (105878) (2020) 1–7.
[4] O. Al-Ahmad, M. Ourak, J.V. Roosbroeck, J. Vlekken, E.V. Poorten, Improved FBG-based shape sensing methods for vascular catheterization treatment, IEEE Robot. Autom. Lett. 5 (3) (2020) 4687–4694.
[5] F. Parent, M. Gérard, F. Monet, S. Loranger, G. Soulez, R. Kashyap, S. Kadoury, Intra-arterial image guidance with optical frequency domain reflectometry shape sensing, IEEE Trans. Med. Imaging 38 (2) (2018) 482–492.
[6] F. Khan, A. Denasi, D. Barrera, J. Madrigal, S. Sales, S. Misra, Multi-core optical fibers with Bragg gratings as shape sensor for flexible medical instruments, IEEE Sens. J. 19 (14) (2019) 5878–5884.
[7] D. Zheng, J. Madrigal, H. Chen, D. Barrera, S. Sales, Multicore fiber-Bragg-grating-based directional curvature sensor interrogated by a broadband source with a sinusoidal spectrum, Opt. Lett. 42 (18) (2017) 3710–3713.
[8] D. Paloschi, K. Bronnikov, S. Korganbayev, A. Wolf, A. Dostovalov, P. Saccomandi, 3D shape sensing with multicore optical fibers: transformation matrices vs Frenet-Serret equations for real-time application, IEEE Sens. J. 21 (4) (2020) 4599–4609.
[9] K. Bronnikov, A. Wolf, S. Yakushin, A. Dostovalov, O. Egorova, S. Zhuravlev, S. Semjonov, S. Wabnitz, S. Babin, Durable shape sensor based on FBG array inscribed in polyimide-coated multicore optical fiber, Opt. Express 27 (26) (2019) 38421–38434.
[10] A. Beisenova, A. Issatayeva, I. Iordachita, W. Blanc, C. Molardi, D. Tosi, Distributed fiber optics 3D shape sensing by means of high scattering NP-doped fibers simultaneous spatial multiplexing, Opt. Express 27 (16) (2019) 22074–22087.
[11] B. Carotenuto, A. Micco, A. Ricciardi, E. Amorizzo, M. Mercieri, A. Cutolo, A. Cusano, Optical guidance systems for epidural space identification, IEEE J. Sel. Top. Quantum Electron. 23 (2) (2016) 371–379.
[12] B. Carotenuto, A. Ricciardi, A. Micco, E. Amorizzo, M. Mercieri, A. Cutolo, A. Cusano, Smart optical catheters for epidurals, MDPI Sens. 18 (7) (2018) 2101.
[13] S. Ambastha, S. Umesh, S. Dabir, S. Asokan, Spinal needle force monitoring during lumbar puncture using fiber Bragg grating force device, J. Biomed. Opt. 21 (11) (2016) 117002.
[14] M. Froggatt, J. Moore, High-spatial-resolution distributed strain measurement in optical fiber with Rayleigh scatter, Appl. Opt. 37 (10) (1998) 1735–1740.
[15] B. Holmstrom, N. Rawal, K. Axelsson, P. Nydahl, Risk of catheter migration during combined spinal epidural block: percutaneous epiduroscopy study, Anesth. Analg. 80 (4) (1995) 747–753.
[16] I. Floris, J. Adam, P. Calderon, S. Sales, Fiber optic shape sensors: a comprehensive review, Opt. Laser Eng. 139 (6) (2021) 106508.
[17] A. Beisenova, A. Issatayeva, S. Korganbayev, C. Molardi, W. Blanc, D. Tosi, Simultaneous distributed sensing on multiple MgO-doped high scattering fibers by means of scattering-level multiplexing, J. Lightwave Technol. 37 (13) (2019) 3413–3421.
[18] C. Shi, X. Luo, P. Qi, T. Li, S. Song, Z. Najdovski, T. Fukuda, H. Ren, Shape sensing techniques for continuum robots in minimally invasive surgery: a survey, IEEE Trans. Biomed. Eng. 64 (8) (2016) 1665–1678.
[19] S. Jäckle, T. Eixmann, H. Schulz-Hildebrandt, G. Hüttmann, T. Pätz, Fiber optical shape sensing of flexible instruments for endovascular navigation, Int. J. Comput. Assist. Radiol. Surg. 14 (12) (2019) 2137–2145.
[20] S. Jäckle, V. García-Vázquez, T. Eixmann, F. Matysiak, F. von Haxthausen, M. Sieren, H. Schulz-Hildebrandt, G. Hüttmann, F. Ernst, M. Kleemann, T. Pätz, Three-dimensional guidance including shape sensing of a stentgraft system for endovascular aneurysm repair, Int. J. Comput. Assist. Radiol. Surg. 15 (2) (2020) 1033–1042.
[21] J. Arkwright, I. Underhill, S. Maunder, N. Blenman, M. Szczesniak, L. Wiklendt, I. Cook, D. Lubowski, P. Dinning, Design of a high-sensor count fibre optic manometry catheter for in-vivo colonic diagnostics, Opt. Express 17 (25) (2009) 22423–22431.

[22] W. Blanc, V. Mauroy, L. Nguyen, S. Bhaktha, P. Sebbah, B. Pal, B. Dussardier, Fabrication of rare earth-doped transparent glass ceramic optical fibers by modified chemical vapor deposition, J. Am. Ceram. Soc. 94 (8) (2011) 2315–2318.
[23] W. Blanc, B. Dussardier, Formation and applications of nanoparticles in silica optical fibers, J. Opt. 45 (6) (2016) 247–254.
[24] S. Kushimoto, S. Yamanouchi, T. Endo, T. Sato, R. Nomura, M. Fujita, D. Kudo, T. Omura, N. Miyagawa, T. Sato, Body temperature abnormalities in non-neurological critically ill patients: a review of the literature, J. Intensive Care 2 (14) (2014) 1–6.
[25] D. Tosi, C. Molardi, W. Blanc, Rayleigh scattering characterization of a low-loss MgO-based nanoparticle-doped optical fiber for distributed sensing, Opt. Laser Technol. 133 (106523) (2021) 1–8.